3D correlative light and electron microscopy of cultured cells using serial blockface scanning electron microscopy

Matthew R. G. Russell[1], Thomas R. Lerner[2], Jemima J. Burden[3], David O. Nkwe[3,5], Annegret Pelchen-Matthews[3], Marie-Charlotte Domart[1], Joanne Durgan[4], Anne Weston[1], Martin L. Jones[1], Christopher J. Peddie[1], Raffaella Carzaniga[1], Oliver Florey[4], Mark Marsh[3], Maximiliano G. Gutierrez[2] & Lucy M. Collinson[1]*

[1] Electron Microscopy Science Technology Platform, The Francis Crick Institute, 1 Midland Road, London NW1 1AT, UK

[2] Host-pathogen Interactions in Tuberculosis Laboratory, The Francis Crick Institute, Mill Hill Laboratory, The Ridgeway, Mill Hill, London NW7 1AA, UK

[3] MRC Laboratory for Molecular Cell Biology, University College London, Gower Street,

London WC1E 6BT, UK

[4] The Babraham Institute, Cambridge, CB22 3AT, UK

[5] Present Address: Department of Biology and Biotechnological Sciences, College of Science, Botswana International University of Science and Technology, Private Bag 16, Palapye, Botswana.

* Corresponding author

Journal of Cell Science • Advance article

Summary statement: We present a new workflow for 3D correlative light and electron microscopy of cell monolayers, and demonstrate application to studies of *M.tuberculosis*-infected cells, HIV-1-infected cells and entotic cell-in-cell structures.

ABSTRACT

The processes of life take place in multiple dimensions, but imaging these processes in even three dimensions is challenging. Here we describe a workflow for 3D correlative light and electron microscopy (CLEM) of cell monolayers using fluorescence microscopy to identify and follow biological events, combined with serial blockface scanning electron microscopy to analyse the underlying ultrastructure. The workflow encompasses all steps from cell culture to sample processing, imaging strategy and 3D image processing/analysis. We demonstrate successful application of the workflow to three studies, each aiming to better understand complex and dynamic biological processes, including bacterial and viral infections of cultured cells and formation of entotic cell-in-cell structures commonly observed in tumours. Our workflow revealed new insight into the replicative niche of *Mycobacterium tuberculosis* in primary human lymphatic endothelial cells, HIV-1 in human monocyte-derived macrophages, and the composition of the entotic vacuole. The broad application of this 3D CLEM technique will make it a useful addition to the correlative imaging toolbox for biomedical research.

INTRODUCTION

Correlative light and electron microscopy (CLEM) is a widely used technique that allows researchers to combine two separate imaging modalities in a manner that overcomes the limitations of each (Muller-Reichert and Verkade, 2014, Muller-Reichert and Verkade, 2012). Fluorescence microscopy (FM) allows identification of tagged macromolecules and analysis of their biological roles within living cells and tissues. However, information is limited by the resolution of the light microscope and by lack of fine structural detail elsewhere in the cell. Electron microscopy (EM) offers much improved resolution and, critically, ultrastructural context, but at the expense of imaging a fixed sample and with a restricted field of view. By combining these two techniques, CLEM makes it possible to target rare and/or dynamic bio-events for structural analysis at high resolution.

EM for CLEM was traditionally performed by manually serial sectioning the sample and imaging each section using a transmission EM (TEM), usually requiring more than 100 sections to image a single cell. However, automated systems based on the scanning EM (SEM) are gaining in popularity. These innovative 'volume EM' techniques (Kremer et al., 2015, Peddie and Collinson, 2014) include array tomography (AT) (Micheva and Smith, 2007, Wacker and Schroeder, 2013), focused ion beam SEM (FIB SEM) (Heymann et al., 2006) and serial blockface SEM (SBF SEM) (Denk and Horstmann, 2004). In AT, sections are cut manually or automatically (Hayworth et al., 2006) and placed in an array on a silicon wafer for large area imaging in the SEM. In FIB SEM a gallium ion beam sputters slices of material from the blockface, whereas in SBF SEM a diamond knife in a miniaturised ultramicrotome removes thin slices from the blockface. In both cases, the revealed surface of the block is imaged using a backscattered electron (BSE) detector, and the process repeated sequentially to build up a stack of images through the volume of the sample.

Previous studies have reported the combination of CLEM workflows with volume EM techniques. Correlative or conjugate AT (CAT) has been applied to map synapses in brain tissue (Oberti et al., 2011, Collman et al., 2015); correlative light and FIB SEM (Lucas et al., 2012, Lucas et al., 2014) has been used to image cells (Murphy et al.,

2011, Beckwith et al., 2015), developing blood vessels in zebrafish (Armer et al., 2009, Bushby et al., 2012) and dendritic spines and synapses in brain tissue (Maco et al., 2013, Bosch et al., 2015, Blazquez-Llorca et al., 2015). Here, we report a correlative workflow for 3D FM to SBF SEM, and demonstrate application to several different biological questions, particularly focusing on the geometry of cell monolayers.

The workflow is illustrated using our recent analysis of primary human lymphatic endothelial cells (hLECs) infected with *Mycobacterium tuberculosis* (Mtb), a newly identified niche for the bacterium in the lymph nodes of patients with tuberculosis (Lerner et al., 2016). In our study, we determined that there were fewer intracellular bacteria when the process of autophagy was inhibited. We hypothesised that the bacteria were growing in autophagosomes, and this was investigated using this 3D CLEM workflow. First, we identified lymphatic endothelial cells that had been transduced with LC3-RFP and also contained EGFP-expressing bacteria. Next, live imaging allowed us to track an infected cell over five days, by which time it was clear that the bacteria were alive, growing and dividing (the EGFP signal was increasing in area) despite being located in an LC3+ compartment, which is conventionally associated with Mtb killing. However, FM did not have sufficient resolution to answer basic questions regarding the nature of the compartment, such as bacterial load, host and bacterial membrane structure, and internal composition of the LC3+ compartment. In addition, we could not be confident that the LC3+ compartment was a continuous structure completely encapsulating the bacteria in all axes.

We applied the same workflow to study entosis, an intriguing example of cell cannibalism in which one live epithelial cell is completely engulfed by another (Overholtzer et al., 2007, Overholtzer and Brugge, 2008). This process leads to the formation of 'cell-in-cell' structures, which are commonly observed in human cancers. Following engulfment, the internalized cell can remain viable for many hours, residing in a single membrane entotic vacuole formed by invagination of the host plasma membrane. The majority of internalized cells are ultimately killed and digested by their host through a process involving a non-canonical function for autophagy proteins and lysosomal degradation (Florey et al., 2011). Entosis is

distinct from other types of macro-endocytic engulfment, such as phagocytosis, as the internalizing cell plays an active role in its own uptake, dependent on adherens junctions and actinomyosin contractility (Overholtzer et al., 2007, Sun et al., 2014). In light of the differences between entosis and other well studied forms of engulfment, and the difficulty in determining whether cells are fully engulfed using light microscopy, we sought to examine the cell-in-cell structures and the entotic vacuole in more detail using 3D CLEM.

Finally, we illustrate how the workflow was applied to a study of human monocyte derived macrophages (MDMs) infected with human immunodeficiency virus type 1 (HIV-1) (Nkwe et al., 2016). HIV-1-infected MDMs accumulate large numbers of virus particles in intracellular plasma membrane-connected compartments (IPMC) (Mlcochova et al., 2013, Deneka et al., 2007). This virus has been proposed to be long-lived and environmentally protected, sequestered away from the host's immune response and possibly antiviral drugs (Sharova et al., 2005, Mlcochova et al., 2013). Whilst IPMCs have been shown to contain mature and immature virus particles, whether they are the main site of HIV assembly, a site of particle storage or a location where engulfed exogenous viruses can accumulate, has been a topic of considerable debate (Welsch et al., 2011, Marsh et al., 2009, Tan and Sattentau, 2013). Understanding the contribution and regulation of this compartment is therefore of great interest, especially as there is increasing evidence that macrophages play an important role in establishing infection in vivo (Sewald et al., 2015) and may also play a role in HIV-associated neurocognitive disorders in patients on antiretroviral therapy (Rappaport and Volsky, 2015). The highly pleomorphic structure of IPMCs was beyond the resolution of the light microscope, so we used our 3D CLEM workflow to identify a macrophage with a prominent IPMC and then imaged through the volume with sufficient resolution to clearly identify ultrastructural features.

RESULTS
A workflow for 3D CLEM using SBF SEM

A significant portion of life sciences research is performed using cells grown in culture. We developed a workflow for 3D correlative analysis of fluorescently-labelled structures in cells cultured on glass coverslips (Fig. 1). The workflow was based on the classic pre-embedding CLEM method (Polishchuk et al., 2000) that moves from LM to TEM, but with modifications to sample preparation and imaging strategies tailored to SBF SEM.

From live-cell imaging to resin-embedded cells

Cells were grown on photo-etched gridded glass bottom dishes, with the coordinates used for recording regions of interest (ROI) (Fig.1A). A diamond scorer or forceps can also be used to mark cell positions on plain glass coverslips. In general, cells were imaged using timelapse confocal microscopy until the biological event occurred, at which point they were chemically fixed by addition of aldehydes to the cell medium. For confocal z-stacks, images were acquired from the whole volume of the cell starting at the coverslip, which was essential for successful 3D FM and 3D EM correlation. A map of the cell location was then created using phase-contrast or brightfield light microscopy over a large field of view (FOV) to show cell shape, cell position in relation to surrounding cells, and the closest number and lines of the grid.

Fluorescence imaging of live (Fig.7) or fixed (Fig.4-6,8) cells was used for correlation with SBF SEM data, depending on the dynamics of the process being studied. Acquisition parameters varied between systems and were dependent on the experimental conditions and fluorophores used (Table S1). In general, we suggest using the highest magnification and highest NA objective available (at least 1024 x 1024 pixel dimensions, zoom 2, line averaging 4, minimal z-section thickness and z-section interval corresponding to half the z-section thickness). Markers for ER, mitochondria and lysosomes may be added to improve FM and EM data alignment, by increasing the number of landmarks.

Following primary fixation, cells were processed into resin using the method of Deerinck and Ellisman (Deerinck et al., 2010), which adds extra heavy metal into the cells for improved conductivity during imaging. Removal of the coverslip from the

polymerised resin block with liquid nitrogen resulted in a monolayer of cells at the blockface, overlaid by a positive cast of the grid (Fig.1B). The region of interest (ROI) was trimmed so that the cell of interest was in the centre of the blockface (Fig.1B), and cut from the block to yield a frustum (truncated square pyramid) 2 mm high with a face of ~500 x 500 μm (Fig.1C, Movie S1). The released frustum was mounted onto an aluminium pin using conductive epoxy glue to aid in charge dissipation during imaging (Fig.1D, Movie S2). The block was mounted with a slight tilt so that the face was ~5º from horizontal to aid the approach to the ROI.

Approach strategy in the SBF SEM

The block was sputter-coated with a thin layer of platinum (Pt) to further aid charge dissipation. The pin was secured in the sample holder and the cell of interest identified (Fig.2A). The diamond knife was aligned parallel to the front edge of the blockface and the height adjusted to the highest corner or edge of the blockface. The slight tilt applied to the blockface during mounting allowed us to approach the cell of interest from one side, so that cutting and imaging conditions were stable prior to starting the imaging run. The coarse approach to the cell was performed with the chamber door open, at 100 nm slice thickness, after which the door was closed and the chamber pumped to ~5 Pa. The cell of interest was relocated at 5 kV using the BSE detector (Fig.2B), and a fine approach performed using 50 nm cuts (Fig.2C). Imaging and cutting conditions were optimised on an adjacent cell before setting up the SBF SEM run.

Imaging strategy

Imaging cell monolayers in the SBF SEM was challenging because of the high proportion of insulating resin. Conductive paths through the sample were therefore few or absent, leading to a build-up of electrons at the sample surface and charging artefacts. Managing electron dose and charging at the specimen surface was therefore critical to acquire high quality data. Charging artefacts were mitigated by balancing a number of inter-dependent imaging parameters. In general, we used a high beam current setting to generate sufficient BSE signal, whilst imaging at low voltage (which also helps limit imaging depth), at a vacuum pressure of ~5-10 Pa (which suppresses charging but worsens the signal-to-noise ratio (SNR)), in

combination with a fast per-pixel dwell time, and use of a small final aperture (Table S2).

For successful serial imaging, it was crucial to balance signal generation with reduced charging and stable cutting. When the electron dose was too high, sectioning artefacts including inconsistent cutting and rippling at the resin surface were visible in empty resin, even when areas containing cellular material continued to section well. Generally, increased section thicknesses tolerated higher electron doses better, at the expense of axial resolution. Under optimal conditions it was possible to attain an axial resolution of 10-15 nm (Fig.3). We demonstrated stable serial imaging at 15 nm section thickness over 1000 slices on a resin block containing B-cells loaded with 200 nm beads (Thaunat et al., 2012). As expected, it took ~13 cuts (mean ± s.e.m. = 13.1 ± 0.42, n = 12 beads from two separate clusters) to section through a single 200 nm bead (Fig.3A). We also achieved stable serial imaging at 10 nm section thickness over 370 slices on a resin block containing Vero E6 cells (Fig.3B; Movie S3).

Overlaying 3D LM and 3D EM data

A typical volume EM dataset consisting of hundreds of slices acquired at 8192 x 8192 pixels can reach well beyond 100 GB. Visualising and processing 'big data' can become a significant problem. We mitigated this by separating the overlay process into two distinct stages: Calculation of the spatial transform using binned images, and subsequent application of the transform to the full resolution images.

In aligning two 3D datasets from different imaging modalities, a six-axis alignment must be considered (x, y, z, pitch, yaw, roll), in addition to scaling and shear. Processing of the sample between LM and EM imaging can also introduce non-linear deformations, which cannot be accounted for with a simple affine transformation. To help correct such effects, we used the BigWarp plugin in Fiji (http://fiji.sc/BigWarp; BigWarp version 2.1.0, Fiji based on ImageJ 1.50e on Windows 10) which harnesses the BigDataViewer system (Pietzsch et al., 2015) allowing efficient handling and display of very large datasets. This is currently the only software that we are aware of that can do such an efficient alignment of two raw 3D datasets, including live transformation as landmarks are repositioned. BigWarp uses a thin plate spline method with manual landmarks to map one dataset

onto another, with the major advantage that the transform is encoded as a small text file containing just the landmark positions. A Fiji script (see https://figshare.com/s/33a422c43fde70ac8580) was written to generate an image stack showing BigWarp landmark locations in 3D. Since the transformation is mathematically well-defined for a given set of landmarks, anyone with access to the raw data files can use the landmarks to immediately view the transformed data and, if necessary, adjust the transform without having to rewrite any image files.

Proof of principle 1: Understanding Mtb environments during intracellular growth

As part of a recent study, we showed that disrupting autophagy inhibited Mtb growth in resting human endothelial lymphocytes. We used FM to identify and follow Mtb-infected cells, and correlated this data with SBF SEM to reveal that Mtb grew inside the autophagosomes in which they were completely encapsulated. SBF SEM allowed us to observe the full cellular microenvironment in which Mtb colonies grew including the compartments in which they were located and the host organelles that interact with them (Lerner et al., 2016). Here, we describe in detail the workflow used to obtain this information, and further analyse the dataset from this cell to reveal new biological information (Fig.4-5). We also describe an extended workflow, linking SBF SEM to TEM, to reveal higher resolution ultrastructural detail from an LC3+ Mtb-compartment in another cell of interest (Fig.6).

Imaging the BSL3 pathogen Mtb required carefully considered, verified safety protocols and specialised equipment, all of which must be contained within a dedicated facility. Our BSL3 laboratory has a confocal microscope equipped with an environmental chamber that enabled live cell imaging of eukaryotic cells infected with Mtb over extended periods of time (routinely up to 12 days), necessary due to the slow growth of the pathogen. HLECs expressing the autophagosomal marker LC3-RFP were infected with EGFP-expressing Mtb and imaged until co-localisation of the bacteria with LC3 was observed (Fig.4A). The cell of interest was followed through sample preparation for SBF SEM as described (Fig.4B-C) and serial images acquired (Fig.4E). Coarse overlay of FM and SBF SEM images (Fig.4D) allowed us to identify individual mycobacteria in a group within the target cell, bound by a perimeter membrane (Fig.4E). The structural resolution of the images was sufficient

to allow segmentation of the Mtb and the surrounding host membrane (Fig.4G). Importantly, 3D CLEM identified morphologically-distinct bacteria that were missed in the initial segmentation because they were more electron-dense than other bacteria in the colony (Fig.4D,F-H, marked in blue). To refine and extend the analysis beyond that shown in (Lerner et al., 2016), 3D FM-EM overlays were created using BigDataViewer and BigWarp (Fig.5D), using Mtb and LC3+ perimeter membranes as landmarks (Fig.5A-C) (Table S5). This precise overlay identified additional LC3+ membrane-whorls inside the compartment that resembled lysosomes or autolysosomes (Fig.5E). We performed new analysis on the resulting models and found that the average Mtb volume was 0.44 μm^3 (n=39) (Table S3), consistent with previously published 2D dimensions, suggesting that there is no growth defect (Cook et al., 2009).

LC3 is known to associate with various compartments, including canonical double-membrane autophagosomes (Mizushima et al., 2002) and non-canonical single-membrane compartments (Sprenkeler et al., 2016 Cell Microbiol). To definitively distinguish single- and double-membranes, and improve our understanding of the LC3+ compartment in which Mtb grow, we introduced a transfer step from SBF SEM to higher resolution TEM. A new cell of interest was selected and imaged by 3D CLEM, and a coarse overlay of the FM and EM images performed, which identified a group of bacilli in another LC3+ compartment (Fig.6A,B). The SBF SEM run was stopped ~30 sections into the compartment. The pin was removed and placed in a standard ultramicrotome. Since the blockface was already polished to a flat surface, having been cut in the SBF SEM (Fig.6C), it was possible to cut complete sections within 1-2 cuts (Fig.6D). The sample was already highly contrasted by the *en bloc* stain, so no post-staining of the TEM sections was required. It was thus possible to inspect a single bacterium in adjacent SBF SEM and TEM sections (Fig.6E,F). Electron tomography (ET) was performed on the TEM sections to achieve the highest possible resolution, and unequivocally identify a single limiting membrane surrounding the group of bacteria (Fig.6H), demonstrating that this particular compartment was not a double-membrane-bound autophagosome.

Proof of principle 2: Visualising cell-in-cell structures formed by entosis

To study entosis by 3D CLEM, MCF10A breast epithelial cells were transfected with the phospholipid phosphatidylinositol 4,5-bisphosphate [$PI(4,5)P_2$] sensor, as a live marker of the plasma membrane, and seeded onto gridded glass bottom dishes where cell-in-cell structures formed. Unlike phagocytosis, where $PI(4,5)P_2$ is lost from phagosomes soon after formation (Botelho et al., 2000), we observed that $PI(4,5)P_2$ remains enriched at both the host and engulfed cell plasma membranes and the entotic vacuole (Fig.7A). Apparent differences in intensity between membranes most likely relate to variable expression levels of the sensor in the cell population rather than $PI(4,5)P_2$ levels. The entotic cell position was recorded using grid maps taken with DIC in live cell conditions. By SBF SEM, the internalized cell appeared morphologically viable with an intact plasma membrane and nucleus, confirming this as a live cell engulfment event (Fig.7B, Movie S4). FM and SBF SEM images were aligned using BigWarp. The first landmarks were placed at the bottom of the cell, at the base of the filopodia (Fig.7C). 21 landmarks in total were selected on the plasma membrane of the cells and the entotic vacuole throughout the volume (Fig.7D, Table S6, Movie S5). The overlaid FM and SBF SEM data confirmed that the entotic vacuole appeared similar in characteristics to plasma membrane (Fig.7E), consistent with retention of $PI(4,5)P_2$. 3D CLEM confirmed that the entotic cell was completely engulfed by the host cell (Fig.7F, Movie S5), which has not been previously observed. Given the limitations of light microscopy in observing and differentiating between the vacuole and plasma membranes, and the possibility of missing gaps through the whole cell volume using 2D electron microscopy; 3D CLEM was the only method that can confirm complete engulfment during entosis.

Proof of principle 3: Insights into HIV trafficking in human monocyte-derived macrophages

To identify and localise MDMs infected with budding-arrested HIV-1 mutants with prominent IPMCs, we used the live-cell stain CellMask™ orange, a fluorescent plasma membrane dye that accesses IPMCs through surface connections (Fig.8A) (Mlcochova et al. 2013). The cell of interest was relocated in the resin block using the maps and FM data (Fig.8B), trimmed (Fig.8C,D) and the first few serial ultrathin

sections collected to assess the quality of the sample and confirm the presence of viral buds by TEM (Fig.8E and magnified insert). The sample was then transferred to the SBF SEM and >300 images were collected. Though SBF SEM images (Fig.8F and magnified insert) were lower resolution than the TEM images (Fig.8E and magnified insert), they had sufficient resolution over a large volume to segment and model the IPMC (whose location was confirmed by coarse overlay of 2D FM data – BigWarp was not used in this case), revealing an intricate network of interconnected membranes (Fig. 8H-I). Manual segmentation of the virus profiles enabled 3D localisation and visualisation of the assembling particles with respect to the IPMC (Fig.8J,K) and cell surface proper (Nkwe et al., 2016). The CellMask^{TM} staining indicated that the IPMC was comprised of two linked domains with distinct morphologies: one compact that opened up to the cell surface via a single narrow channel (Fig.8I,K; arrow); and the second a vast interconnected mesh of channels with virions present throughout, with multiple openings to the cell surface (Fig.8I,K; arrowhead). The two domains were linked by multiple multiple channels of varying diameter, each narrowing at points to less than 100 nm (Fig. 8H, I) (Nkwe et al., 2016). Further quantitative analysis of the 3D model for this paper showed that the two domains not only differ in morphology but also in size and viral contribution (Table S4). More specifically, the domain displaying an interconnected meshwork morphology contributes more than 5 times the area of IPMC membrane when compared to the compact domain, but contains only 1.8 times the number of virus buds, indicating a 3-fold enrichment of budding virus profiles in the compact domain IPMC.

DISCUSSION

We present a workflow for 3D CLEM, from FM to SBF SEM, applied to analyse a range of biological questions that use a monolayer of cultured cells as a model system. At an imaging rate of one cell per day, CLEM analysis starts to become routine and quantitative. When lateral resolution is limiting, for example when the lipid bilayer of a biological membrane must be resolved, we have shown that serial sections can be taken from the blockface during the SBF SEM run for TEM or ET of the same structure.

Our workflow differs from those designed for correlative light and FIB SEM (Karreman et al., Beckwith et al., 2015), since the sample geometry, cutting and imaging conditions differ between the two systems. The FIB SEM is targeted, it is capable of milling very thin slices in the order of ~5 nm, and multiple ROIs can be imaged at the blockface with less severe charging artefacts. The SBF SEM is simpler to set up and cuts faster over a larger area, but slice thickness is routinely set at 25-50 nm and the serial imaging run is more sensitive to charging artefacts (Peddie and Collinson, 2014). However, both techniques are destructive, which is an important consideration since CLEM experiments usually involve 'single-shot' specimens.

In the first study presented here, 3D CLEM revealed new information about the nature of the LC3+ compartment containing Mtb in hLECs (Lerner et al., 2016). New analysis of the original data allowed us to quantify the number of Mtb in the compartment more accurately, demonstrating that 3D CLEM was essential to identify morphologically-distinct bacteria. Further quantitative analysis of the compartment revealed that average Mtb volume was normal, supporting our previous finding that these compartments promote bacterial growth rather than restrict it (Lerner et al., 2016). Future measurement of intracellular Mtb volume using this method could also help to assess the effect of antibiotics, since they are known to affect both bacterial size and morphology (Farnia et al., 2010). We also analysed the content of the Mtb-containing compartment and found additional LC3+ structures that could be influencing bacterial growth, with morphologies reminiscent of lysosomes or autolysosomes. Analysing a second cell with our new 3D CLEM-TEM workflow, we also unequivocally show an Mtb-containing compartment surrounded

by a single LC3+ membrane, also suggestive of an autolysosome or a non-canonical autophagosome.

3D CLEM also provided the first 3D ultrastructural analysis of the large and unusual cell-in-cell structures formed through entosis. Entosis is triggered by loss of matrix attachment, through a recently described engulfment mechanism, and is prevalent in human tumours. The internalised cell is held in a vacuole inside the host cytoplasm that, in an interesting parallel with the Mtb compartment, comprises a single membrane, which becomes LC3+ (Florey et al., 2011). Previously it was not possible to determine whether live entotic cells were fully engulfed, leaving open the possibility that their persistent viability was perhaps due to incomplete internalisation. 3D CLEM has provided the required resolution to distinguish vacuole and plasma membrane through the whole cell volume and allows us to conclude that live cells can be held inside a fully scissioned vacuole. These data also yield new insights into phosphoinositide behaviour during entosis, suggesting that the profile of lipid changes differ in entosis from those in other macro-scale engulfment processes. Unlike phagosomes, which mature quickly upon formation and fuse with lysosomes, the entotic vacuole retains $PI(4,5)P_2$ even after scission. Taken together, these data reveal the existence of an unusual intracellular $PI(4,5)P_2$ positive vacuole compartment. The retention of $PI(4,5)P_2$ and delay in maturation may explain why the internalized cell is able to remain viable even after engulfment and opens up a new line of research into the unique phospholipid dynamics associated with this important live cell engulfment event.

3D CLEM of budding-arrested HIV-1-infected MDMs was perhaps the most challenging of the three proof-of-principle studies, requiring sufficient resolution to detect and trace individual virus budding intermediates over a whole-cell volume. The resulting data allowed high resolution mapping of virus assembly sites and plasma membrane within an IPMC and a full 3D visualisation of this complex compartment. This 3D data was particularly interesting as it was not only in agreement with our previous 2D TEM 'snapshots' of the compartment (Pelchen-Matthews et al. 2012, Mlcochova et al., 2013, Deneka et al. 2007, Nkwe et al., 2016), but also allowed us to understand how the various morphologies previously

described from 2D images of different cells may be connected in a single compartment with morphologically distinct domains. This work extends that reported in Nkwe et al. (2016) by quantifying virus load in the different IPMC domains, indicating a 3-fold enrichment of budding virus profiles in the compact domain, the consequences of which will be investigated in ongoing work. In summary, the mapping virus assembly sites has enabled us to unequivocally demonstrate that the IPMC is a major site of HIV-1 assembly (Nkwe et al., 2016). This workflow provides a robust experimental approach for further investigations into relatively large, intricate and morphologically complex IPMCs and assess their contribution to HIV assembly in macrophages.

Importantly, all three proof of principle studies illustrate the richness of 3D EM datasets, and show how a single dataset can be 'mined' multiple times for biological information. Following publication of the primary study, and deposition of the raw dataset in a public archive such as EMPIAR (Iudin et al., 2016), any scientist will be able to re-analyse the same data to extract further information about the same biological process (as shown here) or even about other biological processes occurring in the same volume. Working in this way will maximise the output from and impact of existing data resources, avoid large-scale expensive duplication of effort in data collection (especially when dealing with precious animal models), centralise multiple datasets collected by different groups from the same biological system to assess reproducibility, build a central resource of 3D datasets that will aid development of image analysis tools, and thus accelerate biomedical discovery.

MATERIALS AND METHODS

Cell culture: Section thickness demonstrations

200 nm microspheres (Invitrogen) coated with antigen were loaded into mouse MD4 B cells as described in (Thaunat et al.). Vero E6 cells were cultured as described in (Limpens et al., 2011).

Cell culture and light microscopy: Mtb-infected cells

The full procedure for Mtb-infected cells was described in (Lerner et al., 2016). Briefly, primary hLECs taken from inguinal lymph nodes (ScienCell Research Laboratories, USA, #2500), were seeded in fibronectin-treated 35 mm glass bottom dishes (e.g. MatTek Corp., USA, # P35G-2-14-CGRD or P35G-2/1.5-14-CGRD or Ibidi μ-Dish$^{35\ mm,\ high}$ Glass Bottom Grid-500) at a density of 30-50% confluence (approx. 10,000 cells) in 500 μl endothelial cell medium (ECM) (ScienCell Research Laboratories, USA, #1001) supplemented with 1% (v/v) endothelial cell growth supplement (ECGS) (ScienCell Research Laboratories, USA, #1052) and 5% (v/v) foetal bovine serum (FBS) (ScienCell Research Laboratories, USA, #0025) at 37°C with 5% CO_2. While still in suspension, 10 μl Premo Autophagy Sensor LC3B-RFP BacMam 2.0 (Life Technologies, USA, #P36236) was added to transduce the cells prior to overnight incubation at 37°C with 5% CO_2. hLEC were then infected with *Mycobacterium tuberculosis* H37Rv constitutively expressing EGFP (as described in (Lerner et al., 2016)). After 5 hours of infection at a multiplicity of infection of 10 bacteria per cell, the MatTek dish was washed three times with PBS and 1 ml ECM medium added containing 10 μl BacMam 2.0 LC3B-RFP to boost transduction; at this point the cells were ready for live cell imaging.

The MatTek dish was securely fastened into a custom made dish holder (in accordance with BSL3 regulations) and put onto the stage of a Leica SP5 AOBS Laser Scanning Confocal Microscope (Leica Microsystems, Germany) with an environmental control chamber (EMBLEM, Germany). Immersion oil used was Cargille Type 37 (Cargille Labs, USA). Images were acquired using scanning mode xyzt with sequential acquisition (see Table S1 for full parameters). Frames were taken every 2 h for the first 12 h, then every 30 min. Z-stacks of five slices were taken at

each time point. Imaging continued for 121.5 h, until Mtb growth in an LC3+ compartment was clear.

The cells were fixed by addition of 4% PFA/2.5% glutaraldehyde in 0.1 M phosphate buffer (PB; pH 7.4) for 24 h at 4°C (a long fixation is necessary for BSL3 regulations). The fixative was then replaced with 0.1 M PB pH 7.4 and the cell of interest was re-located on the microscope using a 10x objective to find the grid-reference and then imaged again at high magnification (63x) to gain the final images to correlate with the electron microscopy images.

Cell culture and light microscopy: Entotic cells

MCF10A cells were cultured in DMEM/F12 (Gibco, 11320-033) supplemented with 5% horse serum (Gibco, 16050-122), 20 ng/mL EGF (Peprotech, AF-100-15), 10 µg/mL insulin (Sigma I9278), 0.5 µg/mL hydrocortisone (Sigma, H0888), 100 ng/µL cholera toxin (Sigma, C8052) and 100 U/mL penicillin and 100 µg/mL streptomycin (Gibco 15140-122). Cells were transfected with the GFP-PLCδ-PH containing plasmid (Addgene 21179) using a Nucleofector II instrument (Lonza) and Lonza nucleofection kit V (Lonza, VCA-1003) with programme T-024, following manufacturer's guidelines, and cultured for 1 day. Transfected cells were re-seeded onto 35mm gridded glass-bottom dishes (MatTek Corp., USA, # P35G-2-14-CGRD) and used the following day.

Live cell images were acquired with a Confocal Zeiss LSM 780 microscope (Carl Zeiss Ltd) at 37°C in a temperature and CO_2 controlled chamber, using Zen software (Carl Zeiss Ltd) (see Table S1 for full parameters). Cells were fixed by adding 8% formaldehyde (Sigma F8775) in 0.2 M PB pH 7.4, in a 1:1 ratio with culture media in the dish. Samples were further fixed in 2.5% glutaraldehyde (Sigma G5882) and 4% formaldehyde in 0.1 M PB pH 7.4 for 30 min at room temperature. Samples were then kept in 1% formaldehyde in 0.1 M PB pH 7.4 and stored at 4°C until processing.

Cell culture and light microscopy: HIV-infected cells

A detailed description of the materials and methods for HIV-1 infected MDMs can be found in (Nkwe et al., 2016). Briefly, stocks of infectious budding-arrested HIV-1 were prepared by transfecting HEK 293T cells, using FuGENE HD (Roche, Welwyn Garden City, UK), with a mixture of mutant virus plasmid and pCMVGag WT. Seven

day old MDMs, grown on coverslips in 24 well plates were infected by spinoculation (centrifugation at 1,300 g and 25˚C for 2 hours) with the rescued mutant virus at 6 focus forming units per cell (spinoculation is not possible with the 35mm photo-etched gridded glass-bottom dishes in the BSL3 environment). MDMs were cultured for 7 more days in Roswell Park Memorial Institute (RPMI) 1640 medium supplemented with 10% human serum, 100 units/ml penicillin, 100 µg/ml streptomycin, 37˚C, 5% CO_2. Infected MDMs were incubated with 5µg/ml CellMask[TM] Orange (Invitrogen Molecular Probes, Paisley, UK) for 10 min at 37˚C before fixation with 4% formaldehyde. Cells were washed in PBS and imaged with a 20x objective on an inverted light microscope (Leica DMIL LED, Leica, Vienna, Austria) to localise cells with prominent IPMCs (see Table S1 for full parameters). Once identified, the cell of interest and its neighbours were marked, by removing a ring of cells surrounding them, using forceps. Further fixation was carried out with 2% formaldehyde and 1.5% glutaraldehyde in 0.1 M sodium cacodylate, prior to further processing.

Sample preparation for electron microscopy

Samples were embedded using a protocol adapted from the NCMIR protocol (Deerinck et al., 2010). Briefly, after fixation, the samples were post-fixed in 2% osmium tetroxide/ 1.5% potassium ferricyanide (v/v) for 1 h on ice, incubated in 1% thiocarbohydrazide in dH_2O (w/v) for 20 min, followed by 2% osmium tetroxide in dH_2O (w/v) for 30 min, washed in dH_2O and incubated overnight in 1% aqueous uranyl acetate at 4°C. Cells were then stained with Walton's lead aspartate for 30 min at 60°C. The coverslips were removed from the dishes after submerging the bottom in methanol for 20 min to soften the glue. The cells were then dehydrated stepwise through an ethanol series in a tin foil container on ice, incubated in a 1:1 propylene oxide/Durcupan resin mixture and embedded in Durcupan ACM® resin according to the manufacturer's instructions (Sigma Aldrich).

Sample mounting

The coverslip was removed from the resin by dipping the block into liquid nitrogen. After localising the ROI at the blockface using the finder grid, the block was cut to fit in the ultramicrotome using a hacksaw, and trimmed with a razorblade to a frustum

(truncated square pyramid) with height ~2 mm and blockface of ~500 µm x 500 µm with the cell of interest located centrally (Fig.1B). Parafilm™ was stretched over the blockface to reduce the risk of losing the frustum, which was then removed by cutting horizontally through the base (~2 mm below the top surface) using a razorblade (Fig.1C, Movie S1). Without touching the top surface, the frustum was dislodged from the parafilm and mounted onto an aluminium pin using conductive epoxy glue (ITW Chemtronics) so the blockface had a small tilt from horizontal (< 5 degrees) (Movie S2). The glue was brought up around the block sides for stability, but care was taken not to allow any of the glue onto the blockface. The glue was hardened at 60°C overnight, and sputter-coated with 2 nm Pt using a Q150R S sputter coater (Quorum Tech).

SBF SEM data collection

SBF SEM data was collected using a 3View2XP (Gatan, Pleasanton, CA) attached to a Sigma VP SEM (Zeiss, Cambridge). The pin was loaded into the SBF SEM. The knife was aligned parallel to the front edge of the block, and then to the highest corner or edge of the blockface with the SEM door open. The cell of interest was identified by adjusting the lighting to see through the Pt coating, using the LM maps and images of the blockface acquired in the ultramicrotome during trimming for reference. A coarse approach was performed by cutting 100 nm sections until the Pt line was a few microns from the cell of interest. The chamber door was then closed and the SEM pumped to ~5 Pa.

Using the BSE detector, an overview image of the whole blockface was acquired at 5 kV. At this voltage, charging effects were visible but it was possible to image through the Pt coat to the cells below, so that the final FOV could be determined. The final approach was performed at 50 nm slice thickness, cutting 10 slices at a time and following the lateral progression of the Pt line towards the cell of interest.

The SEM imaging conditions for each dataset are presented in Table S2. For cutting analysis (Fig.3A), 15 nm cuts were taken from a B cell sample containing 200 nm beads. Two clusters of beads in two separate areas in a cell were quantified. The number of cuts taken through each bead were counted and averaged to confirm slice thickness.

TEM image acquisition

The SBF SEM run was stopped once the structure of interest had been identified, using LM maps and FM images as a reference. The pin was removed from the SBF SEM and placed in a UC7 ultramicrotome (Leica Microsystems). The cut face was aligned to the diamond knife as closely as possible. 100 nm thick sections were cut, collected on formvar-coated slot grids, and imaged in a Tecnai G2 Spirit BioTwin TEM (FEI Company) using an Orius CCD camera (Gatan Inc.). Tilt series were acquired from ±70° using an Ultrascan CCD camera (Gatan Inc.) and Inspect 3D software (FEI Company). Tomograms were reconstructed using the back projection algorithm in IMOD software (Kremer et al., 1996).

Image processing for 10 nm dataset from Vero E6 cells

To reduce noise and improve image contrast, the extracted image stack was batch processed using Adobe Photoshop to convert it to 8 bit greyscale, apply a 1 pixel Gaussian blur, and resharpen with an unsharp mask (60%, 20 pixel radius; then 50% 5 pixel radius). The image stack was then imported into Fiji (Schindelin et al., 2012), cropped to the area of interest, and contrast was normalised across all slices.

Overlay of 3D LM and 3D EM datasets

For 3D LM-EM alignment, both image stacks were opened in Fiji. The LM image stack was usually a multi-channel confocal z-stack from a single time-point. The native EM file format (Gatan Digital Micrograph '.dm4' format) was opened using the Bio-Formats importer (http://www.openmicroscopy.org/site/support/bio-formats5.1/). If the image stack size was larger than the available memory it was opened as a virtual stack. This was rescaled in Fiji, ensuring that the rescaled EM pixel resolution was higher than the native LM pixel resolution.

In the BigWarp plugin, the EM stack was set as 'target' and the LM stack as 'moving' dataset. 'Landmark mode' was used to add at least four pairs of corresponding points within the LM and EM data. Further points were added to refine the transform and correct for non-linear deformations caused by sample processing. The graphical user interface of BigWarp was particularly useful for these steps since the transformation can be applied live, and even continuously adjusted by dragging a

landmark. It was also useful for visualising feature correlation in orthogonal and oblique planes to fine-tune landmark placement; the EM dataset could be aligned to the plane of the Pt layer, which was coplanar with the coverslip in the LM dataset (hence why it was advisable to acquire a full confocal stack from the coverslip upwards). It was important to choose points that were well separated in all three dimensions to minimise angular errors in the rotations. The final transformations were saved in BigWarp, which could then be applied to the full resolution data to produce the final overlay. The landmark table could be exported as a small textfile containing sufficient information to recreate the full alignment.

For manual segmentation and 3D model generation of Mtb and HIV-1 datasets, EM image stacks were converted to 8-bit greyscale tiff format and a 0.5 or 1 pixel Gaussian blur applied, then aligned and manually segmented using Amira software (FEI Company). HIV budding profiles were manually placed using TrakEM2 (Schindelin et al., 2012), then their co-ordinates were extracted using a python script (courtesy of Albert Cardona) and imported into Amira for visualisation. For 3D rendering of the entotic cell dataset, we used the ClearVolume plugin in Fiji (http://fiji.sc/ClearVolume) (Royer et al., 2015). The SBF SEM image was inverted and the platinum signal subtracted to aid visualisation in 3D.

Competing interests

No competing interests declared.

References

ARMER, H. E., MARIGGI, G., PNG, K. M., GENOUD, C., MONTEITH, A. G., BUSHBY, A. J., GERHARDT, H. & COLLINSON, L. M. 2009. Imaging transient blood vessel fusion events in zebrafish by correlative volume electron microscopy. *PLoS One,* 4**,** e7716.

BECKWITH, M. S., BECKWITH, K. S., SIKORSKI, P., SKOGAKER, N. T., FLO, T. H. & HALAAS, O. 2015. Seeing a Mycobacterium-Infected Cell in Nanoscale 3D: Correlative Imaging by Light Microscopy and FIB/SEM Tomography. *PLoS One,* 10**,** e0134644.

BLAZQUEZ-LLORCA, L., HUMMEL, E., ZIMMERMAN, H., ZOU, C., BURGOLD, S., RIETDORF, J. & HERMS, J. 2015. Correlation of two-photon in vivo imaging and FIB/SEM microscopy. *J Microsc,* 259**,** 129-36.

BOSCH, C., MARTINEZ, A., MASACHS, N., TEIXEIRA, C. M., FERNAUD, I., ULLOA, F., PEREZ-MARTINEZ, E., LOIS, C., COMELLA, J. X., DEFELIPE, J., MERCHAN-PEREZ, A. & SORIANO, E. 2015. FIB/SEM technology and high-throughput 3D reconstruction of dendritic spines and synapses in GFP-labeled adult-generated neurons. *Front Neuroanat,* 9**,** 60.

BOTELHO, R. J., TERUEL, M., DIERCKMAN, R., ANDERSON, R., WELLS, A., YORK, J. D., MEYER, T. & GRINSTEIN, S. 2000. Localized biphasic changes in phosphatidylinositol-4,5-bisphosphate at sites of phagocytosis. *J Cell Biol,* 151**,** 1353-68.

BUSHBY, A. J., MARIGGI, G., ARMER, H. E. & COLLINSON, L. M. 2012. Correlative light and volume electron microscopy: using focused ion beam scanning electron microscopy to image transient events in model organisms. *Methods Cell Biol,* 111**,** 357-82.

COLLMAN, F., BUCHANAN, J., PHEND, K. D., MICHEVA, K. D., WEINBERG, R. J. & SMITH, S. J. 2015. Mapping synapses by conjugate light-electron array tomography. *J Neurosci,* 35**,** 5792-807.

COOK, G. M., BERNEY, M., GEBHARD, S., HEINEMANN, M., COX, R. A., DANILCHANKA, O. & NIEDERWEIS, M. 2009. Physiology of mycobacteria. *Adv Microb Physiol,* 55**,** 81-182, 318-9.

DEERINCK, T. J., BUSHONG, E., THOR, A. & ELLISMAN, M. H. 2010. NCMIR methods for 3D EM: A new protocol for preparation of biological specimens for serial block-face SEM. *Microscopy* [Online], 6-8. Available: http://ncmir.ucsd.edu/sbfsem-protocol.pdf.

DENEKA, M., PELCHEN-MATTHEWS, A., BYLAND, R., RUIZ-MATEOS, E. & MARSH, M. 2007. In macrophages, HIV-1 assembles into an intracellular plasma membrane domain containing the tetraspanins CD81, CD9, and CD53. *J Cell Biol,* 177**,** 329-41.

DENK, W. & HORSTMANN, H. 2004. Serial block-face scanning electron microscopy to reconstruct three-dimensional tissue nanostructure. *PLoS Biol,* 2**,** e329.

FARNIA, P., MOHAMMAD, R. M., MERZA, M. A., TABARSI, P., ZHAVNERKO, G. K., IBRAHIM, T. A., KUAN, H. O., GHANAVEI, J., FARNIA, P., RANJBAR, R., POLESCHUYK, N. N., TITOV, L. P., OWLIA, P., KAZAMPOUR, M., SETAREH, M., SHEIKOLSLAMI, M., MIGLIORI, G. B. & VELAYATI, A. A. 2010. Growth and cell-division in extensive (XDR) and extremely drug resistant (XXDR) tuberculosis strains: transmission and atomic force observation. *Int J Clin Exp Med,* 3**,** 308-14.

FLOREY, O., KIM, S. E., SANDOVAL, C. P., HAYNES, C. M. & OVERHOLTZER, M. 2011. Autophagy machinery mediates macroendocytic processing and entotic cell death by targeting single membranes. *Nat Cell Biol,* 13**,** 1335-43.

HAYWORTH, K., KASTHURI, N., SCHALEK, R. & LICHTMAN, J. 2006. Automating the Collection of Ultrathin Serial Sections for Large Volume TEM Reconstructions. *Microscopy and Microanalysis,* 12**,** 86-87.

HEYMANN, J. A., HAYLES, M., GESTMANN, I., GIANNUZZI, L. A., LICH, B. & SUBRAMANIAM, S. 2006. Site-specific 3D imaging of cells and tissues with a dual beam microscope. *J Struct Biol,* 155**,** 63-73.

IUDIN, A., KORIR, P. K., SALAVERT-TORRES, J., KLEYWEGT, G. J. & PATWARDHAN, A. 2016. EMPIAR: a public archive for raw electron microscopy image data. *Nat Methods,* 13**,** 387-8.

KARREMAN, M. A., MERCIER, L., SCHIEBER, N. L., SOLECKI, G., ALLIO, G., WINKLER, F., RUTHENSTEINER, B., GOETZ, J. G. & SCHWAB, Y. 2016. Fast and precise targeting of single tumor cells in vivo by multimodal correlative microscopy. *J Cell Sci,* 129**,** 444-56.

KREMER, A., LIPPENS, S., BARTUNKOVA, S., ASSELBERGH, B., BLANPAIN, C., FENDRYCH, M., GOOSSENS, A., HOLT, M., JANSSENS, S., KROLS, M., LARSIMONT, J. C., MC GUIRE, C., NOWACK, M. K., SAELENS, X., SCHERTEL, A., SCHEPENS, B., SLEZAK, M., TIMMERMAN, V., THEUNIS, C., R, V. A. N. B., VISSER, Y. & GUERIN, C. J. 2015. Developing 3D SEM in a broad biological context.

KREMER, J. R., MASTRONARDE, D. N. & MCINTOSH, J. R. 1996. Computer visualization of three-dimensional image data using IMOD. *J Struct Biol,* 116**,** 71-6.

LERNER, T. R., DE SOUZA CARVALHO-WODARZ, C., REPNIK, U., RUSSELL, M. R., BOREL, S., DIEDRICH, C. R., ROHDE, M., WAINWRIGHT, H., COLLINSON, L. M., WILKINSON, R. J., GRIFFITHS, G. & GUTIERREZ, M. G. 2016. Lymphatic endothelial cells are a replicative niche for Mycobacterium tuberculosis. *J Clin Invest,* 126**,** 1093-108.

LIMPENS, R. W., VAN DER SCHAAR, H. M., KUMAR, D., KOSTER, A. J., SNIJDER, E. J., VAN KUPPEVELD, F. J. & BARCENA, M. 2011. The transformation of enterovirus replication structures: a three-dimensional study of single- and double-membrane compartments. *MBio,* 2.

LUCAS, M. S., GUENTHERT, M., GASSER, P., LUCAS, F. & WEPF, R. 2014. Correlative 3D imaging: CLSM and FIB-SEM tomography using high-pressure frozen, freeze-substituted biological samples. *Methods Mol Biol,* 1117**,** 593-616.

LUCAS, M. S., GUNTHERT, M., GASSER, P., LUCAS, F. & WEPF, R. 2012. Bridging microscopes: 3D correlative light and scanning electron microscopy of complex biological structures. *Methods Cell Biol,* 111**,** 325-56.

MACO, B., HOLTMAAT, A., CANTONI, M., KRESHUK, A., STRAEHLE, C. N., HAMPRECHT, F. A. & KNOTT, G. W. 2013. Correlative in vivo 2 photon and focused ion beam scanning electron microscopy of cortical neurons. *PLoS One,* 8**,** e57405.

MARSH, M., THEUSNER, K. & PELCHEN-MATTHEWS, A. 2009. HIV assembly and budding in macrophages. *Biochemical Society Transactions,* 37**,** 185-189.

MICHEVA, K. D. & SMITH, S. J. 2007. Array tomography: a new tool for imaging the molecular architecture and ultrastructure of neural circuits. *Neuron,* 55**,** 25-36.

MIZUSHIMA, N., OHSUMI, Y. & YOSHIMORI, T. 2002. Autophagosome formation in mammalian cells. *Cell Struct Funct,* 27**,** 421-9.

MLCOCHOVA, P., PELCHEN-MATTHEWS, A. & MARSH, M. 2013. Organization and regulation of intracellular plasma membrane-connected HIV-1 assembly compartments in macrophages. *BMC Biol,* 11**,** 89.

MULLER-REICHERT, T. & VERKADE, P. 2012. Introduction to correlative light and electron microscopy. *Methods Cell Biol,* 111**,** xvii-xix.

MULLER-REICHERT, T. & VERKADE, P. 2014. Preface. Correlative light and electron microscopy II. *Methods Cell Biol,* 124**,** xvii-xviii.

MURPHY, G. E., NARAYAN, K., LOWEKAMP, B. C., HARTNELL, L. M., HEYMANN, J. A., FU, J. & SUBRAMANIAM, S. 2011. Correlative 3D imaging of whole mammalian cells with light and electron microscopy. *J Struct Biol,* 176**,** 268-78.

NKWE, D.O., PELCHEN-MATTHEWS, A., BURDEN, J.J., COLLINSON, L.M., & MARSH, M. 2016. The intracellular plasma membrane-connected compartment in the assembly of HIV-1 in human macrophages. *BMC Biol,* 14, 50.

OBERTI, D., KIRSCHMANN, M. A. & HAHNLOSER, R. H. 2011. Projection neuron circuits resolved using correlative array tomography. *Front Neurosci,* 5**,** 50.

OVERHOLTZER, M. & BRUGGE, J. S. 2008. The cell biology of cell-in-cell structures. *Nat Rev Mol Cell Biol,* 9**,** 796-809.

OVERHOLTZER, M., MAILLEUX, A. A., MOUNEIMNE, G., NORMAND, G., SCHNITT, S. J., KING, R. W., CIBAS, E. S. & BRUGGE, J. S. 2007. A nonapoptotic cell death process, entosis, that occurs by cell-in-cell invasion. *Cell,* 131**,** 966-79.

PEDDIE, C. J. & COLLINSON, L. M. 2014. Exploring the third dimension: Volume electron microscopy comes of age. *Micron,* 61**,** 9-19.

PIETZSCH, T., SAALFELD, S., PREIBISCH, S. & TOMANCAK, P. 2015. BigDataViewer: visualization and processing for large image data sets. *Nat Meth,* 12**,** 481-483.

POLISHCHUK, R. S., POLISHCHUK, E. V., MARRA, P., ALBERTI, S., BUCCIONE, R., LUINI, A. & MIRONOV, A. A. 2000. Correlative Light-Electron Microscopy Reveals the Tubular-Saccular Ultrastructure of Carriers Operating between Golgi Apparatus and Plasma Membrane. *The Journal of Cell Biology,* 148**,** 45-58.

RAPPAPORT, J. & VOLSKY, D. J. 2015. Role of the macrophage in HIV-associated neurocognitive disorders and other comorbidities in patients on effective antiretroviral treatment. *J Neurovirol,* 21**,** 235-41.

ROYER, L. A., WEIGERT, M., GUNTHER, U., MAGHELLI, N., JUG, F., SBALZARINI, I. F. & MYERS, E. W. 2015. ClearVolume: open-source live 3D visualization for light-sheet microscopy. *Nat Meth,* 12**,** 480-481.

SCHINDELIN, J., ARGANDA-CARRERAS, I., FRISE, E., KAYNIG, V., LONGAIR, M., PIETZSCH, T., PREIBISCH, S., RUEDEN, C., SAALFELD, S., SCHMID, B., TINEVEZ, J. Y., WHITE, D. J., HARTENSTEIN, V., ELICEIRI, K., TOMANCAK, P. & CARDONA, A. 2012. Fiji: an open-source platform for biological-image analysis. *Nat Methods,* 9**,** 676-82.

SEWALD, X., LADINSKY, M. S., UCHIL, P. D., BELOOR, J., PI, R., HERRMANN, C., MOTAMEDI, N., MUROOKA, T. T., BREHM, M. A., GREINER, D. L., SHULTZ, L. D., MEMPEL, T. R., BJORKMAN, P. J., KUMAR, P. & MOTHES, W. 2015. Retroviruses use CD169-mediated trans-infection of permissive lymphocytes to establish infection. *Science,* 350**,** 563-7.

SHAROVA, N., SWINGLER, C., SHARKEY, M. & STEVENSON, M. 2005. Macrophages archive HIV-1 virions for dissemination in trans. *Embo j,* 24**,** 2481-9.

SPRENKELER, E. G., GRESNIGT, M. S. & VAN DE VEERDONK, F. L. 2016. LC3-associated phagocytosis: a crucial mechanism for antifungal host defence against Aspergillus fumigatus. *Cell Microbiol*.

SUN, Q., CIBAS, E. S., HUANG, H., HODGSON, L. & OVERHOLTZER, M. 2014. Induction of entosis by epithelial cadherin expression. *Cell Res,* 24**,** 1288-98.

TAN, J. & SATTENTAU, Q. J. 2013. The HIV-1-containing macrophage compartment: a perfect cellular niche? *Trends Microbiol,* 21**,** 405-12.

THAUNAT, O., GRANJA, A. G., BARRAL, P., FILBY, A., MONTANER, B., COLLINSON, L., MARTINEZ-MARTIN, N., HARWOOD, N. E., BRUCKBAUER, A. & BATISTA, F. D. 2012. Asymmetric segregation of polarized antigen on B cell division shapes presentation capacity. *Science,* 335**,** 475-9.

WACKER, I. & SCHROEDER, R. R. 2013. Array tomography. *J Microsc,* 252**,** 93-9.

WELSCH, S., GROOT, F., KRAUSSLICH, H. G., KEPPLER, O. T. & SATTENTAU, Q. J. 2011. Architecture and regulation of the HIV-1 assembly and holding compartment in macrophages. *J Virol,* 85**,** 7922-7.
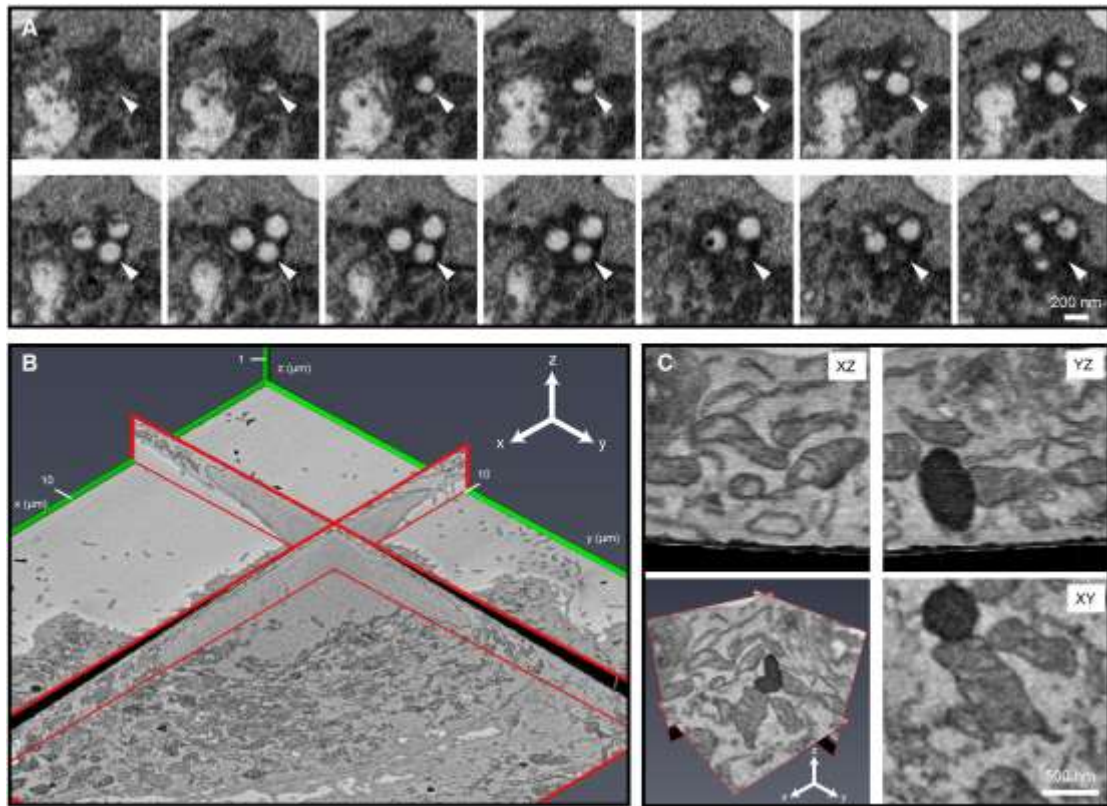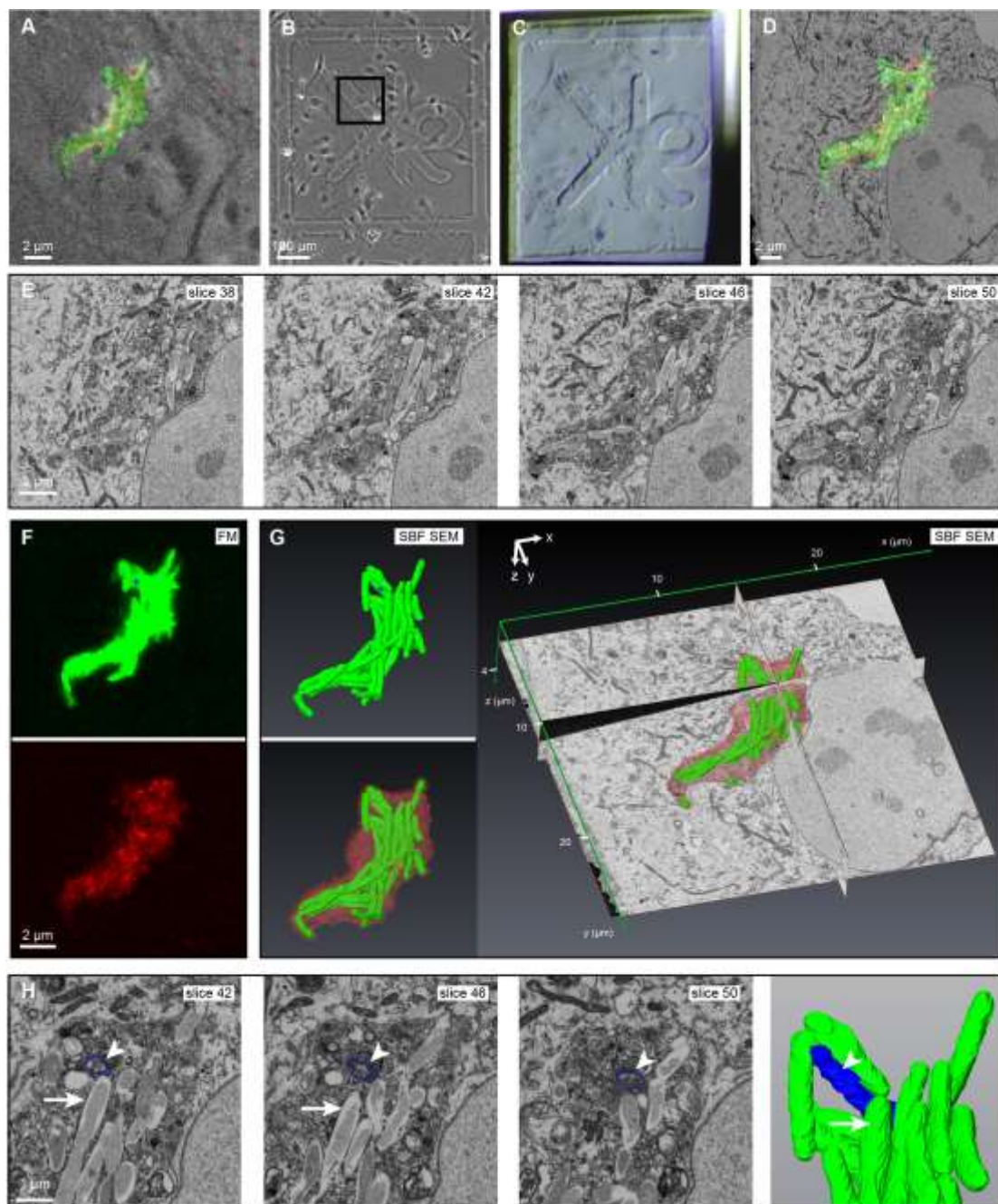
Figures
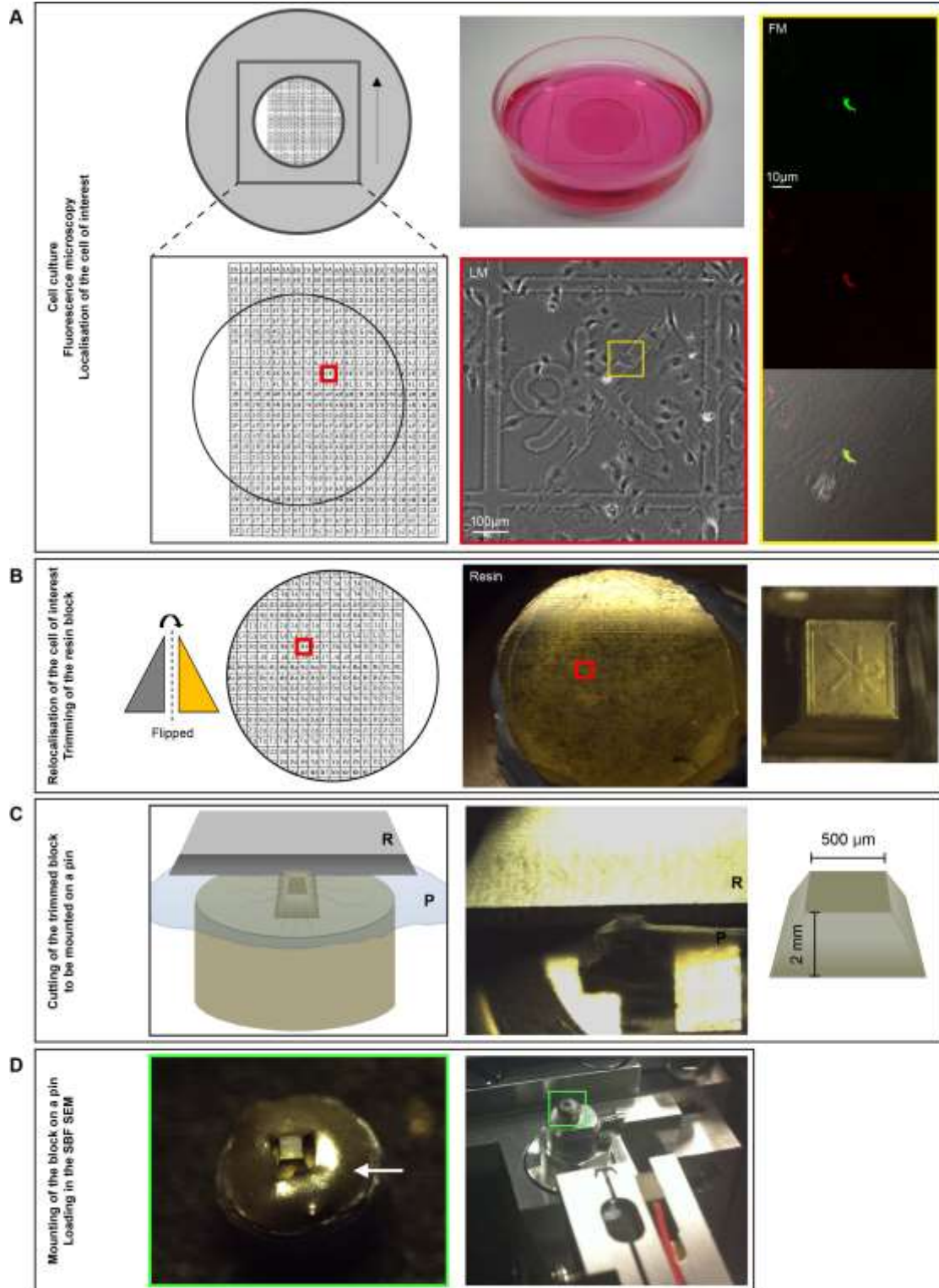
Figure 1. Workflow for sample preparation from live cell imaging to resin embedded cells. A) Left panel: Diagram of gridded glass-bottom dishes (MatTek Corp. # P35G-2-14-CGRD) with cell position indicated by red box. Middle panel: Brightfield image of cell of interest (yellow inset) at grid co-ordinate 9K. Right panel: Confocal fluorescence images were then acquired. B) Following resin-embedding, the coverslip was removed, leaving an inverted cast of the grid on top of a monolayer of embedded cells. The cell of interest was relocated (red inset) and trimmed (right panel). C) The frustum was covered with parafilm (P) and removed with a razorblade (R) (right panel) (Movie S1). D) This was mounted onto an aluminium pin using conductive epoxy glue (left panel- white arrow) (Movie S2), and secured in the SBF SEM sample holder (right panel - green inset).
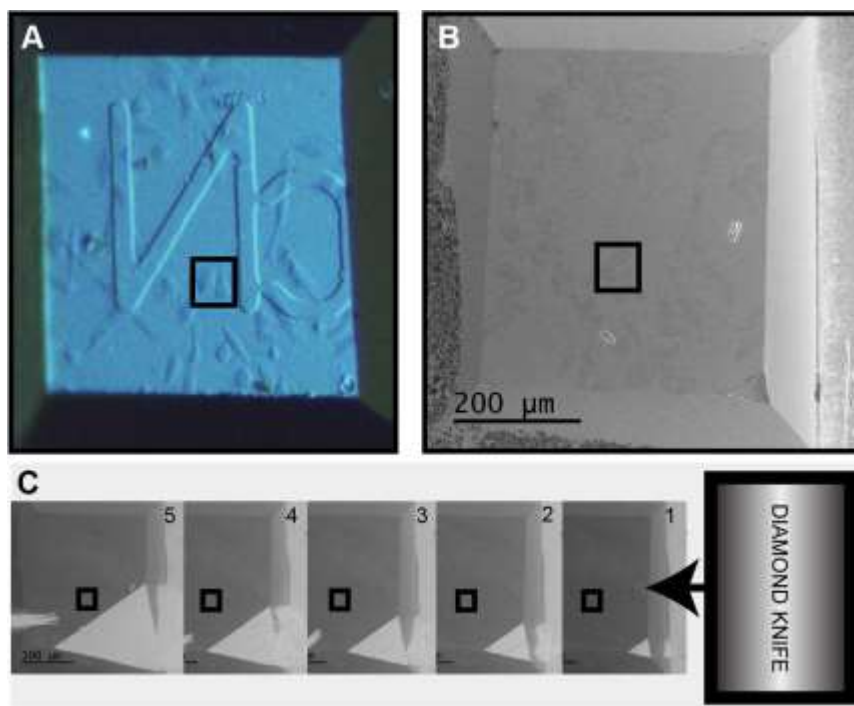
Figure 2. Approach strategy in the SBF SEM. A) The cell of interest (black box) was relocated at the blockface. B) The cells were visible through the Pt layer imaging at 5 kV using the BSE detector. C) The diamond knife was aligned to the highest point of the blockface and the coarse approach performed at 100 nm slice thickness.

Figure 3. Demonstration of stable ultrathin cutting in the SBF SEM. A) SBF SEM of mouse MD4 B cells containing antigen-coated 200 nm beads (Thaunat et al., 2012) cut at 15 nm section thickness and imaged at a pixel size of 15 nm. One of the two bead clusters quantified is shown in 14 consecutive slices (white arrows). B) SBF SEM of Vero E6 cells cut at 10 nm section thickness and imaged at a pixel size of 10 nm (Movie S3). C) Panels show orthoslices from a 2 x 2 x 2 µm cube (bottom left panel) extracted from the dataset shown in B, demonstrating isotropic voxel resolution throughout the volume.

Figure 4. 3D CLEM reveals the subcellular location of Mtb in lymphatic endothelial cells. A-G) Data from (Lerner et al., 2016) is shown to illustrate in detail the workflow used to acquire this data. A) Overlay of GFP-Mtb (green) and LC3-RFP (red) onto a phase contrast image of the infected cell. B) Location map of the cell of interest. C) The grid was transferred to the blockface during embedding, and the block trimmed

and mounted for SBF SEM. The coarse approach cuts have started to clean away the Pt-coat at the right side of the block. D) Coarse overlay of the FM onto an SBF SEM image mid-run to confirm the structure of interest is in the FOV. E) SBF SEM images through the Mtb colony. G) SBF SEM segmentation/reconstruction; the Mtb (green) and perimeter membrane (red) were segmented and modelled with reference to the coarse overlay (D) and FM (F, maximum intensity projections). H) Electron-dense bacterium segmented in blue (arrowhead in H and asterisk in D,F,G) compared with electron-lucent bacterium (arrow).
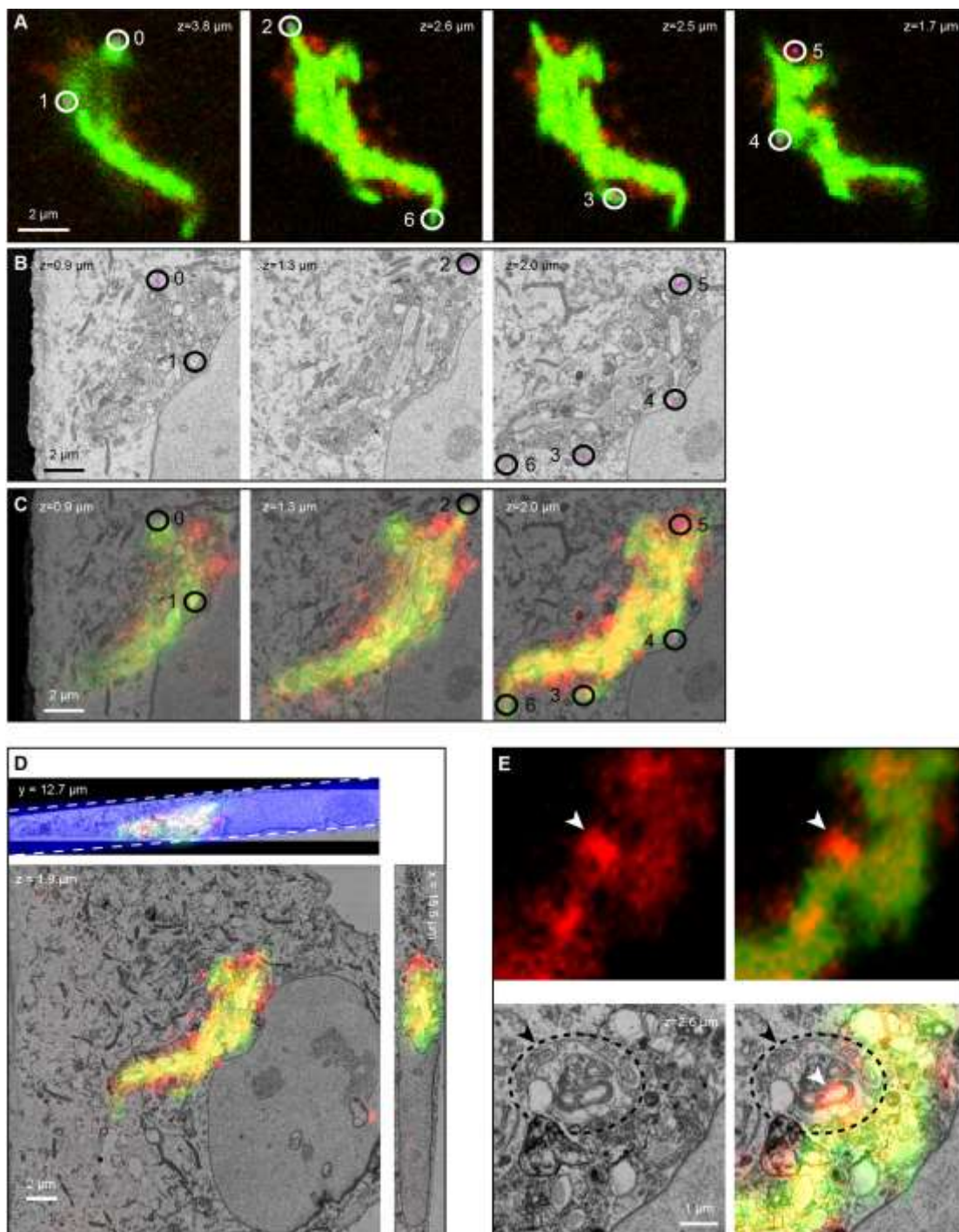
Figure 5. Fine alignment of 3D LM and 3D EM data using BigDataViewer and BigWarp. New analysis of the dataset used for (Lerner et al., 2016). Landmarks were placed (A-C) to generate the fine alignment (D), which could then be used to identify

an LC3+ membrane whorl (E). A) Raw fluorescence slices, with GFP-Mtb (green) and LC3-RFP (red). B) SBF SEM slices. C) Overlay after BigWarp transformation of the fluorescence stack using the landmarks shown. D) XZ plane shows the tilt of the platinum layer (equating to the coverslip) with respect to the horizontal plane of the SBF SEM data. The inclined blue rectangle demarcates a slice through the phase contrast image volume, showing its coplanarity with the platinum layer. E) Membrane rich LC3+ whorl. Panels A-C, E, and the XZ and ZY planes of panel D; snapshots of the BigWarp graphical user interface, with annotations except for the magenta dots added later.
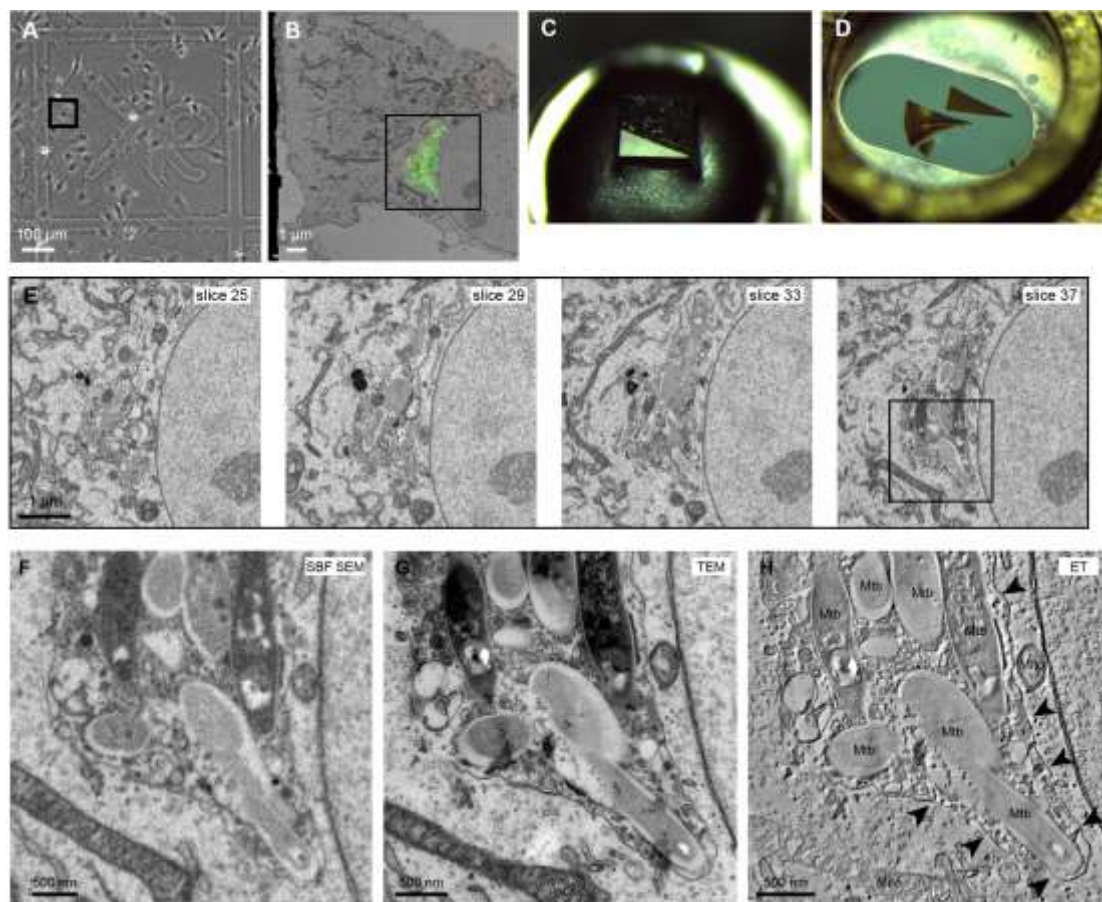
Figure 6. Complementing SBF SEM with high resolution TEM images of the same structure. A) Location map of the cell of interest, and B) Coarse overlay of the FM onto an SBF SEM image mid-run to confirm the structure of interest is in the FOV. C) The block was then removed from the SBF SEM, and D) Serial sections collected for TEM on a formvar-coated slot grid. Using this technique, it was possible to follow the same structure from E-F) SBF SEM to G) TEM. H) High resolution images were acquired by electron tomography (ET), showing the single perimeter membrane (black arrowheads) and individual bacilli (Mtb) within the compartment. Mito - mitochondria.
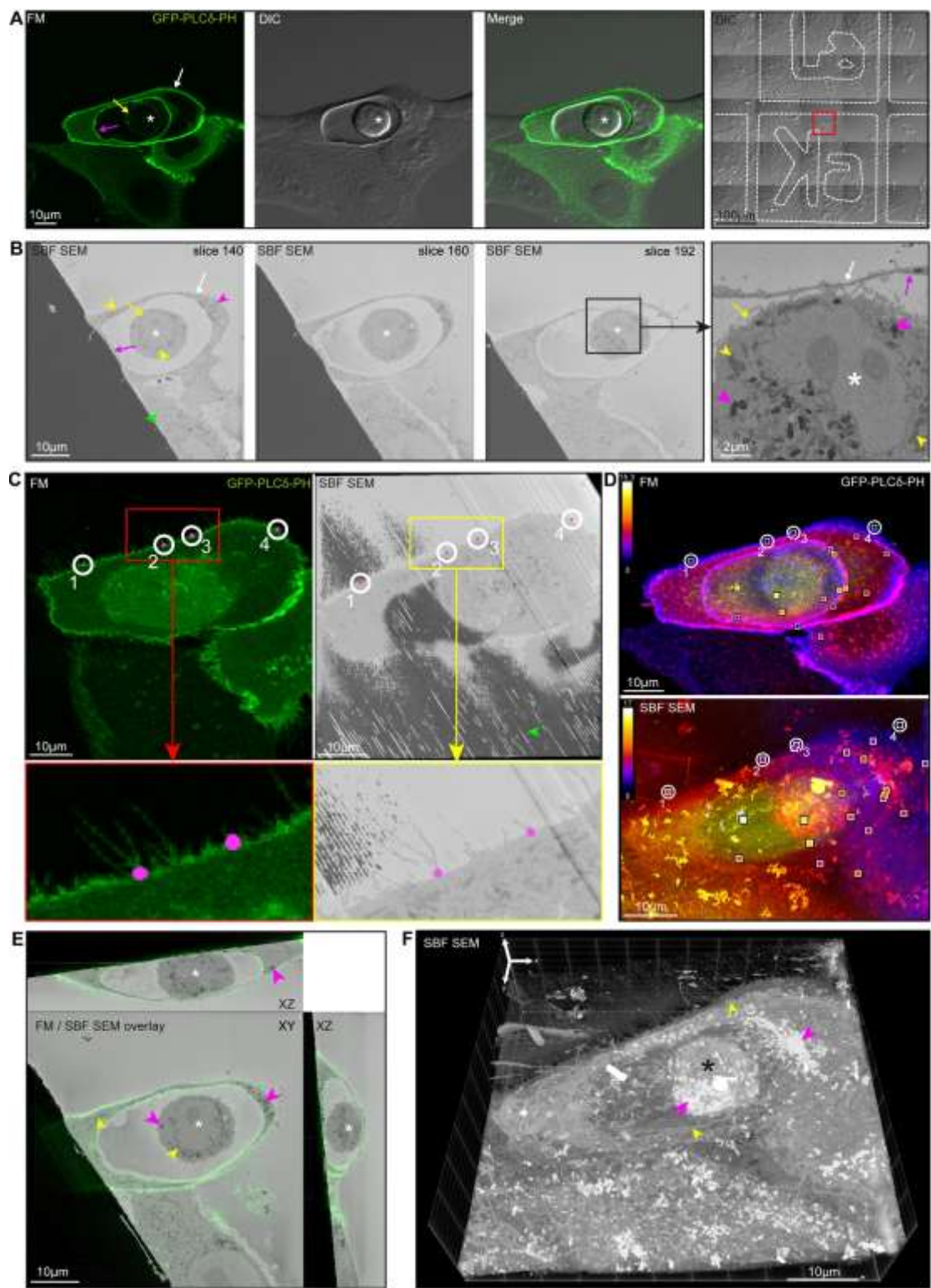
Figure 7. 3D CLEM of a cell-in-cell structure formed by entosis. A) MCF10A breast epithelial cells were transfected with GFP-PLCð-PH (green), which is expressed at both the host and engulfed cell plasma membranes and the entotic vacuole. Cell of interest (red box) was identified in live cell conditions. B) SBF SEM images through entosed cell (Movie S4). C) FM and SBF SEM data were aligned using BigWarp. The GFP-PLCð-PH image (left) and oblique slice through the EM dataset (right) show the position of 4 landmarks using filopodia at the bottom of the cell (insets). D) In total, 21 landmarks were selected on the plasma membrane of the cells and entotic vacuole (Movie S5) shown in depth-coded maximum intensity projections (top: GFP-PLCð-PH, bottom: SBF SEM). Pixel colour denotes the z position at which the maximum intensity in the stack is found. The landmarks are shown as white squares with an inset colour corresponding to the depth position of the landmark. The colourbar indicates the depth in μm. E) Overlay of the resliced GFP-PLCð-PH (green) image stack and the SBF SEM stack using BigWarp, shown in all three orthoslices. F) 3D reconstruction of the SBF SEM stack showing the entotic cell within its host cell. The SBF SEM image was inverted and the platinum signal subtracted to aid visualisation in 3D (Movie S5). Asterisk: Entotic cell. White arrow: host cell plasma membrane. Yellow arrow: engulfed cell plasma membrane. Magenta arrow: entotic vacuole. Yellow arrowhead: mitochondria. Magenta arrowhead: lipid vacuole. Green arrowhead: platinum.
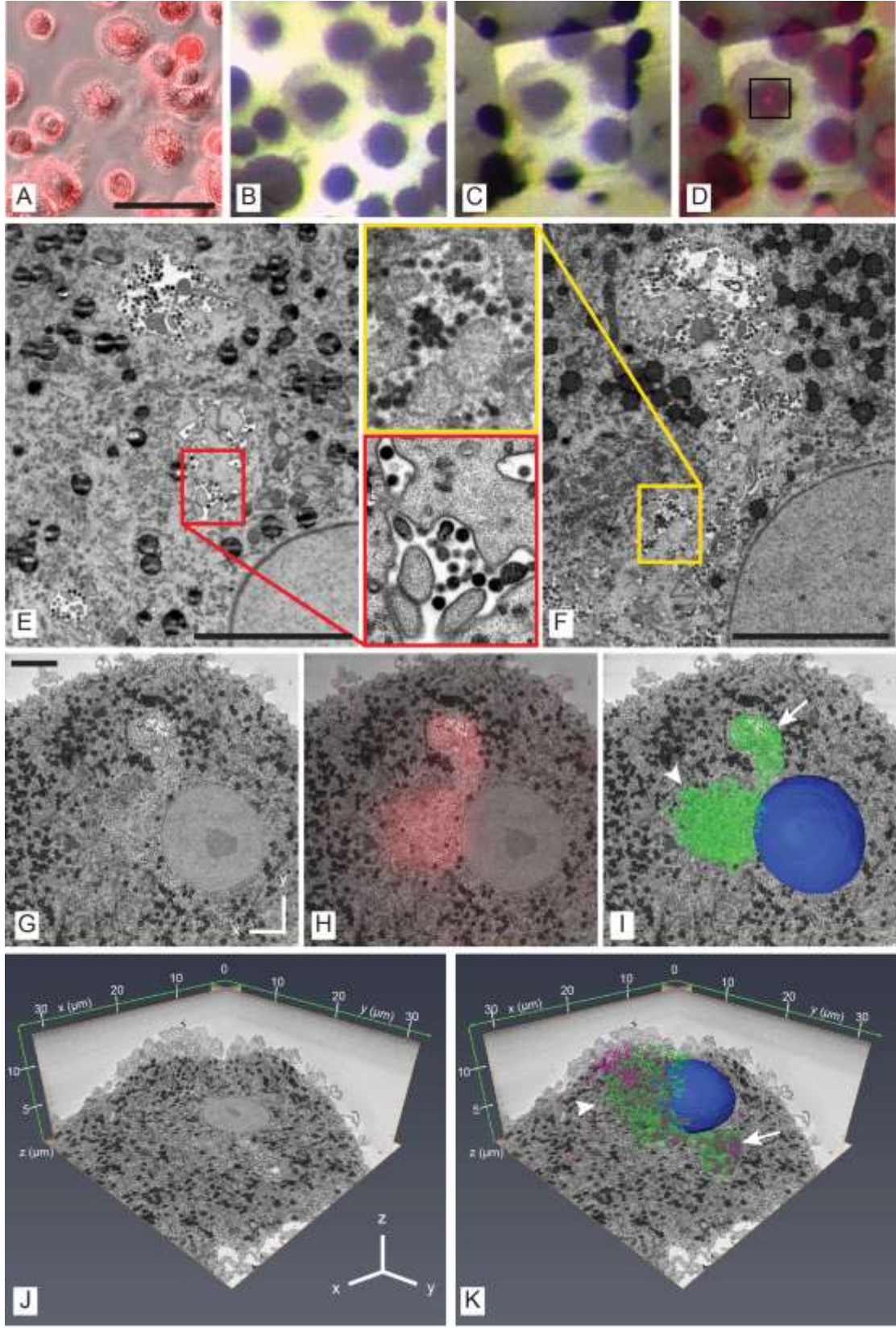
Figure 8. 3D CLEM of HIV-1-infected MDMs. MDMs were infected with budding-arrested HIV-1 mutant virus (Nkwe et al., 2016) and cells with prominent IPMCs were identified by enrichment of CellMask[TM] labelling. A) Widefield FM of IPMC labelling overlaid over a phase contrast image of the cell of interest, bar: 100 µm. B) Resin blockface with cell of interest after processing for SBF SEM, trimmed (C) and overlaid with FM (D). E) TEM of infected cell, bar: 5 µm. F) SBF SEM of matching region (x, y), bar: 5 µm. G) SBF SEM image of cell of interest, bar: 5 µm. H) CellMask[TM] widefield FM image overlaid onto SBF SEM image. I) 3D reconstruction of IPMC (green) and nucleus (blue) overlaid onto SBF SEM image. J) xy, xz and yz orthoslices from SBF SEM data. K) 3D reconstructions of arrested HIV-1 assembly sites (purple), IPMC (green) and nucleus (blue) projected over xy, xz and yz orthoslices from SBF SEM data. I) and K) arrow: compact domain, arrowhead: convoluted domain.
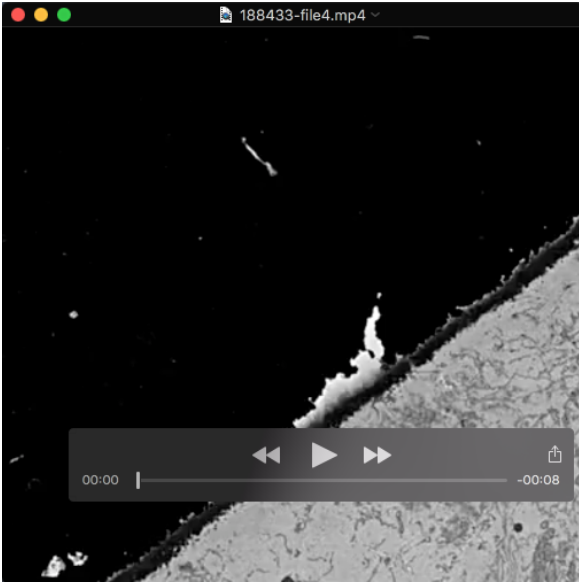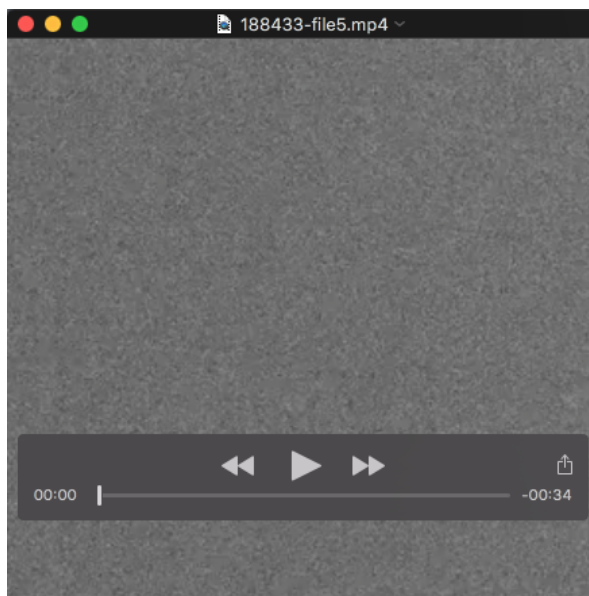
Table S1. Fluorescence light microscopy imaging parameters
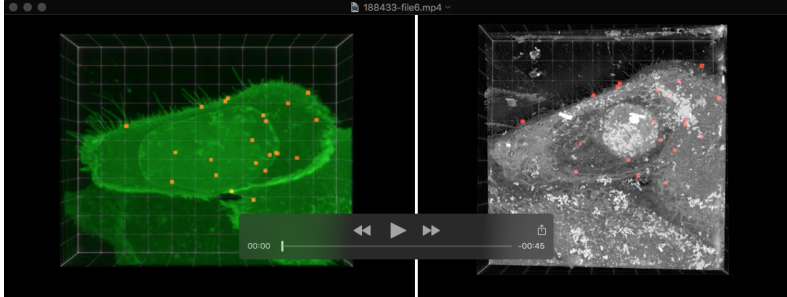
	Fig 4-5, Mtb (Lerner et al., 2016)	Fig 6, Mtb	Fig 7, Entosis	Fig 8, HIV (Nkwe et al., 2016)	Recommended
Live-/Fixed-cell imaging	Live and fixed confocal	Fixed confocal	Live confocal	Fixed widefield	Live and fixed confocal
Objective lens	63x	63x	40x	20x	40x or 63x
NA	1.4	1.4	1.4	0.3	1.4
Pinhole	1 AU, 95.4 µm	1 AU, 95.4 µm	1 AU, 32 µm	n/a	1 AU
Pixel dimensions	1024 x 1024	1024 x 1024	512 x 512	1392 x 1040	1024 x 1024
Zoom	2	1	2.2	n/a	1 or 2
Line averaging	2	4	1	n/a	4
Pixel dwell time	2.1 µs (400 Hz)	2.1 µs (400 Hz)	2.55 µs	n/a	-
Pixel size (µm)	0.12	0.24	0.189	0.46	Nyquist sampling
Optical section thickness (µm)	0.771	0.771	1.7	n/a	set by pinhole (≈ 0.7 µm for 1 AU)
Number of slices	5	1	50	n/a	for whole cell volume
Step size (µm)	1.19	n/a	0.373	n/a	(1/2 of optical section thickness)
HFW (xy µm)	123.02 x 123.02	246.03 x 246.03	96.92 x 96.92	640.32 x 478.4	-
Volume (xyz µm)	123.02 x 123.02 x 5.95	n/a	96.92 x 96.92 x 18.63	n/a	-

NA – numerical aperture of the objective lens
AU – Airy unit
HFW – horizontal field width
n/a – not applicable

Table S2. SBF SEM imaging parameters

	Fig 3A, MD4 Cell 15 nm cuts	Fig 3B-C, Vero Cell 10 nm voxel	Fig 4-5, Mtb (Lerner et al., 2016)	Fig 6, Mtb	Fig 7, Entosis	Fig 8, HIV (Nkwe, et al., 2016)
Vacuum (Pa)	High Vacuum	5	10	10	6	5
Voltage (kV)	2	2	1.8	1.8	2	2
Aperture (μm)	30	30	20	20	20	20
High current mode	No	No	Yes	Yes	Yes	Yes
Pixel dwell time (μs)	2	3	2	2	2	2
Pixel dimensions	2048 x 2048	8192 x 8192	8192 x 8192	8192 x 8192	8192 x 8192	8192 x 8192
Lateral pixel size (nm)	15	10	3	3.1	7	4
Slice thickness (nm)	15	10	50	50	50	50
Slices	1000	200	68	37	341	300
Volume (xyz μm)	30.7 x 30.7 x 15	81.9 x 81.9 x 2	24.3 x 24.3 x 3.4	25.3 x 25.3 x 1.85	57.1 x 57.1 x 17.05	32.8 x 32.8 x 15

Slice thickness – SBF SEM microtome thickness setting
Slices – number of slices in the dataset

Table S3. Mtb 3D reconstruction model quantitation

Mtb	Mtb Volume (μm^3)	Closest distance to surrounding membrane (nm)
1	0.497	271*
2	0.440	271*
3	0.454	345
4	0.283	866
5	0.549	271*
6	0.346	271*
7	0.396	271*
8	0.371	271*
9	0.703	271*
10	0.606	271*
11	0.430	271*
12	0.421	857
13	0.528	271*
14	0.299	347
15	0.386	271*
16	0.470	271*
17	0.318	271*
18	0.394	610
19	0.297	271*
20	0.469	271*
21	0.404	277
22	0.515	271*
23	0.824	445
24	0.361	655
25	0.346	271*
26	0.370	271*
27	0.385	539
28	0.354	271*
29	0.315	852
30	0.332	271*
31	0.432	574
32	1.018	452
33	0.442	271*
34	0.436	639
35	0.364	728
36	0.298	495
37	0.412	271*
38	0.386	271*
39	0.521	271*

Average volume	0.440	

*The real proximity of bacteria shown as 271 nm is equal to or less than this value (since the surrounding membrane was originally segmented as a 270 nm thick object, with the outer face following the electron density of the surrounding membrane, in order to prevent artefactual holes appearing in the surface, see Lerner et al., 2016).

Table S4. IPMC 3D reconstruction model quantitation

	IPMC Membrane area		Virus buds		Virus buds/μm^2 of membrane
	Area μm^2	%	number	% of total	
Whole IPMC	1,444	-	15,624	-	10.8
Compact domain (Fig.8I,K; arrow)	223	15.5	5,674	36.3	25.4
Convoluted domain (Fig.8I,K; arrowhead)	1,220	84.5	9,950	63.7	8.2

Table S5. Mtb BigWarp landmarks

	Landmark positions (µm)					
	Moving (LM)			Target (SBF SEM)		
Landmark	**x**	**y**	**z**	**x**	**y**	**z**
Pt-0	72.265	63.175	3.821	13.848	6.176	0.988
Pt-1	70.266	65.604	3.821	15.707	10.222	0.792
Pt-2	69.530	62.601	2.617	17.287	5.407	1.312
Pt-3	72.738	69.392	2.500	10.887	14.861	2.051
Pt-4	69.749	67.094	1.704	15.442	12.102	1.981
Pt-5	70.355	63.577	1.640	15.686	6.388	2.000
Pt-6	75.106	70.211	2.748	7.079	15.329	2.108

Table S6. Entosis BigWarp landmarks

| Landmark† | Landmark positions (μm) | | | | | |
| | Moving (LM) | | | Target (SBF SEM) | | |
	x	y	z	x	y	z
Pt-0	45.571	38.328	2.551	26.316	15.651	5.370
Pt-1	52.014	36.194	2.309	32.520	13.018	4.223
Pt-2	71.733	34.783	1.921	51.385	9.352	1.157
Pt-3	27.016	42.888	2.648	8.992	21.646	8.339
Pt-4	52.990	59.062	2.890	36.781	34.734	6.125
Pt-5	51.402	36.719	5.309	32.061	13.587	5.839
Pt-6	38.215	56.713	3.852	21.936	33.877	8.569
Pt-9	58.704	61.538	7.133	43.687	36.518	8.361
Pt-10	38.360	49.570	13.668	22.756	26.681	15.878
Pt-11	63.257	50.245	11.002	48.633	22.205	9.360
Pt-12	64.647	49.555	10.498	48.925	21.330	8.776
Pt-13	74.746	41.195	7.467	56.124	16.466	4.787
Pt-14	61.223	40.107	6.502	41.726	14.423	5.857
Pt-15	67.434	37.173	6.208	46.493	12.282	4.690
Pt-16	69.843	50.849	7.879	52.136	25.513	6.441
Pt-17	49.153	55.442	10.986	34.916	30.961	13.056
Pt-18	47.958	51.469	14.437	33.846	26.778	13.835
Pt-19	64.692	49.753	6.390	48.341	22.692	5.663
Pt-21	58.479	46.449	8.516	40.833	21.811	7.961
Pt-22	59.399	52.308	8.053	42.403	26.206	7.988
Pt-23	61.707	54.182	6.749	45.715	28.706	6.835
Pt-24	62.077	41.364	9.538	44.828	15.580	7.828

†Landmarks 7, 8 and 20 were removed during refinement of the alignment